Structural and Magnetic Properties of a New Type of Ordered Oxygen-Deficient Perovskite, $KMnVO_4$

H. Ben Yahia,[†] E. Gaudin,*[,†] C. Lee,[‡] M.-H. Whangbo,[‡] and J. Darriet[†]

ICMCB, CNRS, Université Bordeaux 1, 87 avenue du Dr. A. Schweitzer, 33608 Pessac Cedex France, and Department of Chemistry, North Carolina State University, Raleigh, North Carolina 27695-8204

Received February 15, 2007. Revised Manuscript Received July 11, 2007

A new ternary vanadate $KMnVO_4$ was prepared by a solid-state reaction and was shown to be a new type of ordered oxygen-deficient perovskite $ABO_{3-\delta}$ with $\delta = 1/3$. Its formula can be rewritten as $(K_2,Mn)[Mn,V_2]O_8\square_1$. An ordered distribution of potassium and manganese atoms in the A site and of vanadium and manganese atoms in the B site is observed. The manganese atoms are in distorted octahedral and tetrahedral sites, whereas all of the vanadium atoms form VO_4^{3-} tetrahedra. This oxide contains four different types of high-spin Mn^{2+} ions in equal number. Magnetic susceptibility and specific heat measurements as well as spin dimer analysis show that substantial antiferromagnetic spin-exchange interactions occur primarily among three of the four different types of Mn^{2+} ions, and the fourth Mn^{2+} ion remains paramagnetic down to 2 K.

1. Introduction

Oxides of general formulas ABO_3 and A_2BO_4 represent a major part of solid-state oxide chemistry. Perovskite oxides ABO_3 have been extensively studied because of a large variety of their physical/structural properties and their compositional flexibility to accommodate almost every element in the periodic table. The perovskite structures are grouped into cubic and the hexagonal perovskite structures, both of which can be generated by stacking close-packed AO_3 layers and subsequently filling the octahedral sites between the adjacent layers with B cations. When modified layers are included in the stacking sequence, new structural variations of the perovskite structure result.[1] A cubic or pseudocubic perovskite can be nonstoichiometric because of A-site cation or oxygen vacancies. The typical range of oxygen deficiency in the nonstoichiometric perovskite $ABO_{3-\delta}$ is $0 < \delta \leq 0.5$. Oxygen vacancies created in the perovskite structure can be ordered. For example, in the case of $\delta = 0.5$, the vacancy ordering leads to the brownmillerite Ca_2FeAlO_5,[2] the $Ca_2Mn_2O_5$-type structure,[3] or $La_2Ni_2O_5$.[4] Other ordered oxygen-deficient perovskites are known for different values of δ,[5−15] in particular, for $\delta = 1/3$.[16] The ultimate end in the reduction of the ABO_3 perovskite is exemplified by $LaNiO_2$.[17] The search for a new structural variation of the perovskite structure continues to be an interesting challenge.

Recently, phosphates and vanadates of the formula $AA'BO_4$ (B = P, V; A′ = 3d transition metal; A = alkaline) have received much attention since the discovery of the promising insertion/de-insertion of lithium in $LiFePO_4$.[18] $AA'PO_4$ oxides crystallize largely in four structural types, that is, the olivine,[19] maricite,[20] stuffed-tridymite,[21] and zeolite-ABW type structures,[22] but the ternary vanadates $LiMVO_4$ (M = transition metal) crystallize in the Na_2CrO_4[23] or spinel-type structure.[24] In our search for ternary vanadates $AMnVO_4$ (A = Na, K, Ag, Cu) we prepared a new compound $KMnVO_4$ that we found to represent a new type of ordered oxygen-deficient perovskite $ABO_{3-\delta}$ with $\delta = 1/3$. In this work, the synthesis and structural/magnetic property characterizations of $KMnVO_4$ are described.

* To whom correspondence should be addressed. Email: gaudin@icmcb-bordeaux.cnrs.fr. Fax: (+33)540002761. Phone: (+33)540006328.
[†] Université Bordeaux.
[‡] North Carolina State University.

(1) Mitchell, R. H., *Perovskites Modern and Ancient*; Almaz Press Inc: Ontario, Canada, 2002.
(2) Colville, A. A.; Geller, S. *Acta Crystallogr.* **1971**, *B27*, 2311.
(3) Poepplemeier, K. R.; Leonowicz, M. E.; Longo, J. M. *J. Solid State Chem.* **1982**, *44*, 89.
(4) Alonso, J. A.; Martinez-Lope, M. J. *Mater. Sci. Forum* **1996**, *228*, 747.
(5) Caignert, V.; Nguyen, N.; Hervieu, M.; Raveau, B. *Mater. Res. Bull.* **1985**, *20*, 479.
(6) Michel, C.; Er-Rhako, L.; Raveau, B. *Mater. Res. Bull.* **1985**, *20*, 667.
(7) Rao, C. N. R.; Raveau, B. *Transition Metal Oxides*; VCH Publishers: New York, 1995.
(8) Troyanchuk, I. O.; Mantyskaya, O. S.; Pastushonok, S. N.; Shapovalova, E. F.; Virchenko, V. A. *Crystallogr. Rep.* **1996**, *41*, 797.
(9) Anderson, M. T.; Poeppelmeier, K. R.; Zhang, J. P.; Fran, H. J.; Marks, L. D. *Chem. Mater.* **1992**, *4*, 1305.
(10) Gormenazo, A.; Weller, M. T. *J. Mater. Chem.* **1993**, *3*, 771.
(11) Greenwood, K. B.; Searjeant, G. M.; Poeppelmeier, K. R. *Chem. Mater.* **1995**, *7*, 1335.
(12) Zhu, W. J.; Hor, P. H. *J. Solid State Chem.* **1995**, *120*, 208.
(13) Pack, M. J.; Gormezano, A.; Weller, M. T. *Chem. Mater.* **1997**, *9*, 1547.
(14) González-Calbet, J. M.; Sayagués, J.; Vallet-Regí, M. *Solid State Ionics* **1989**, *32/33*, 721.
(15) González-Calbet, J. M.; Vallet-Regí, M. *J. Solid State Chem.* **1987**, *68*, 266.
(16) Grenier, J. C.; Darriet, J.; Pouchard, M.; Hagenmuller, P. *Mater. Res. Bull.* **1976**, *11*, 1226.
(17) Levitz, P.; Crespin, M.; Gatineau, L. *J. Chem. Soc., Faraday Trans.* **1983**, *79*, 1195.
(18) Pahdi, A. K.; Nanjundaswamy, K. S.; Goodenough, J. B. *J. Electrochem. Soc.* **1997**, *144*, 1188.
(19) Geller, S.; Durand, J. L. *Acta Crystallogr.* **1960**, *13*, 325.
(20) Le Page, Y.; Donnay, G. *Can. Mineral.* **1977**, *15*, 518.
(21) Konnert, J. H.; Appleman, D. E. *Acta Crystallogr.* **1978**, *B34*, 391.
(22) Gatehouse, B. M. *Acta Crystallogr.* **1989**, *C45*, 1674.
(23) Nimmo, J. K. *Acta Cryst.* **1981**, *B37*, 431.
(24) Bernier, J. C.; Poix, P.; Michel, A. *Bull. Soc. Chim. Fr.* **1963**, 445.

10.1021/cm070452b CCC: $37.00
Published on Web 10/25/2007

Table 1. Crystallographic Data and Structure Refinement for $KMnVO_4$

formula	$KMnVO_4$
cryst color	yellow
mol wt (g mol^{-1})	209
cryst syst	monoclinic
space group	$P2_1/n$
params	$a = 12.081(7)$, $b = 5.645(2)$, $c = 23.804(12)$ Å; $\beta = 103.45(2)°$
V(Å^3)	1579(2) Å^3
Z	16
density$_{calcd}$ (g cm^{-3})	3.516(5)
cryst shape	block
T (K)	298
diffractometer	Enraf−Nonius Kappa CCD
monochromator	oriented graphite
radiation	Mo Kα ($\lambda = 0.71069$ Å)
scan mode	CCD scan
$h\ k\ l$ ranges	$-21 < h < 18$, $-10 < k < 7$, $-42 < l < 43$
θ_{min}, θ_{max} (deg)	5, 40
linear abs coeff	6.486 mm^{-1}
abs correction	Gaussian
T_{min}/T_{max}	0.483/0.688
No. of reflns	41 278
R_{int}	0.0612
No. of independent reflns	9753
reflns used ($I > 3\sigma(I)$)	6818
refinement	F^2
F(000)	1584
R factors	R(F)/wR(F^2) = 0.0304/0.0733
No. of refined params	254
GOF	1.31
weighting scheme	$w = 1/(\sigma^2(I) + 0.0009I^2)$
diff. Fourier residues (e$^-$/Å^3)	[-0.72, +1.22]

2. Experimental Section

2.1. Synthesis. $KMnVO_4$ was prepared by solid-state reactions from a stoichiometric mixture of KVO_3 and MnO. (KVO_3 was obtained by heating a 1:1 mixture of K_2CO_3 and V_2O_5 at 550 °C for 6 h.) The mixture was put in a gold tube, which was sealed under a vacuum in a silica tube and then heated at 450 °C for 6 h and at 700 °C for 36 h. Grinding and further heating of the mixture at 750 °C for 24 h led to $KMnVO_4$, as monitored by X-ray diffraction. Single crystals of $KMnVO_4$ were prepared by fast-heating the starting stoichiometric mixture at 950 °C and then by slowly decreasing the temperature at a rate of 2 °C/h to 800 °C and at a rate of 10 °C/h to room temperature. The crystals have a yellow color.

2.2. Magnetic Susceptibility and Specific Heat Measurements. Magnetic susceptibility was measured on powder sample with a SQUID magnetometer in a temperature range from 2 to 320 K under the applied magnetic field of 5 kOe. Specific heat measurements were performed on a $KMnVO_4$ pellet using a PPMS Quantum Design in a temperature range from 2 to 100 K.

2.3. X-ray Diffraction Measurements. A crystal suitable for single-crystal X-ray diffraction was selected on the basis of the size and sharpness of the diffraction spots. Data collection was carried out on an Enraf-Nonius Kappa CCD diffractometer using Mo Kα radiation. Data processing and all of the refinements were performed with the JANA2000 program package.[25] A Gaussian-type absorption correction was applied, and the shape was determined with the video microscope of the Kappa CCD. Details about data collection are summarized in Table 1.

2.4. Structural Refinement. The extinction conditions observed for $KMnVO_4$ agree with the $P2_1/n$ space group. Most of the atomic positions were found by direct method using the *sir97* program.[26]

(25) Petříček, V., Dušek, M. Jana 2000 program, *Inst. Phys. Acad. Sci.* Czech Republik, Prague 1998.

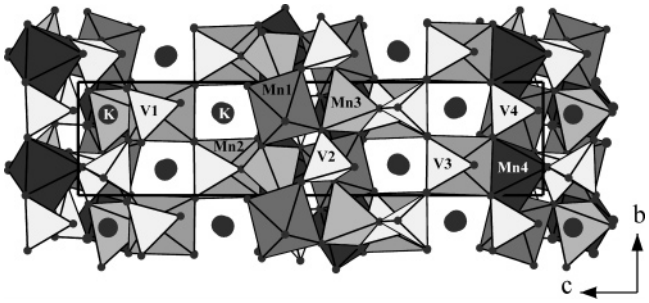

Figure 1. Projection view of the structure of $KMnVO_4$ on the (100) plane.

Table 2. Atomic Coordinates and Equivalent Isotropic Displacement Parameters for $KMnVO_4$

	atoms	x	y	z	U_{eq}(Å^2)
site B	Mn1	0.82354(2)	0.24114(4)	0.441643(12)	0.00894(6)
	Mn2	0.55987(2)	0.23481(4)	0.682563(11)	0.00765(6)
	V1	0.76666(3)	0.75043(5)	0.345541(13)	0.00746(7)
	V2	0.13559(3)	0.27321(5)	0.463837(13)	0.00759(7)
	V3	0.38596(2)	0.27248(5)	0.207757(12)	0.00632(6)
	V4	0.50481(2)	0.27255(5)	0.429752(12)	0.00665(6)
site A	Mn3	0.99521(2)	0.77983(5)	0.424076(13)	0.01036(7)
	Mn4	0.38590(2)	0.25918(5)	0.561929(12)	0.01011(7)
	K1	0.30508(4)	0.78492(8)	0.435752(19)	0.01744(11)
	K2	0.87867(4)	0.76243(7)	0.19183(2)	0.01738(11)
	K3	0.26738(4)	0.27113(7)	0.314432(18)	0.01290(10)
	K4	0.94384(4)	0.28224(8)	0.31348(2)	0.02187(14)
	O1	0.22459(11)	0.1180(2)	0.52017(6)	0.0125(3)
	O2	0.35029(11)	0.6556(2)	0.55434(6)	0.0124(3)
	O3	0.80879(12)	0.0352(2)	0.36414(6)	0.0137(4)
	O4	0.00444(12)	0.1322(2)	0.45036(7)	0.0168(4)
	O5	0.55846(11)	0.4996(2)	0.61322(6)	0.0127(4)
	O6	0.11946(11)	0.5769(2)	0.47788(6)	0.0115(3)
	O7	0.85518(11)	0.5560(2)	0.39432(6)	0.0117(3)
	O8	0.45451(13)	0.2490(2)	0.49008(6)	0.0147(4)
	O9	0.57138(12)	0.9704(2)	0.74905(6)	0.0127(4)
	O10	0.77501(13)	0.6824(3)	0.27941(6)	0.0184(4)
	O11	0.73998(11)	0.2229(2)	0.68737(6)	0.0131(3)
	O12	0.56933(12)	0.4832(2)	0.75056(6)	0.0129(4)
	O13	0.51778(12)	0.9893(2)	0.60871(6)	0.0133(4)
	O14	0.18679(15)	0.2480(3)	0.40587(7)	0.0232(5)
	O15	0.37460(11)	0.2791(2)	0.65047(6)	0.0120(3)
	O16	0.05592(13)	0.7680(3)	0.35068(6)	0.0174(4)

With anisotropic displacement parameters, the final residual factors converged to the value R(F) = 0.0304 and wR(F^2) = 0.0733 for 254 refined parameters and 6818 observed reflections with difference Fourier residues in the range between −0.72 and +1.22 eÅ^{-3} (Table 1). The refined atomic positions and anisotropic displacement parameters (ADPs) are given in Table 2 and the supplementary Table S1, respectively (Supporting Information).[27]

3. Results and Discussion

3.1. Crystal Structure. A projection view of the structure of this new derivative of the ABO_3 perovskite structure with the drawing of the oxygen polyhedra around all of the transition metals is displayed in Figure 1. Projection views on the (100) and (010) planes with only the oxygen polyhedra around the B cations are also presented in parts a and b of Figure 2, respectively. For comparison, a projection view of an ideal cubic perovskite ABO_3 on the (001) plane is also shown in part c of Figure 2, where the A cations occupy the

(26) Altomare, A.; Burla, M. C.; Camalli, M.; Cascarano, G. L.; Giacovazzo, C.; Guagliardi, A.; Moliterni, A. G. G.; Polidori, G.; Spagna, R. *J. Appl. Crystallogr.* **1999**, *32*, 115.

(27) Details may be obtained from Fachinformationszentrum Karlsruhe, D−76344 Eggenstein-Leopoldshafen (Germany), by quoting the Registry No. CSD−416551

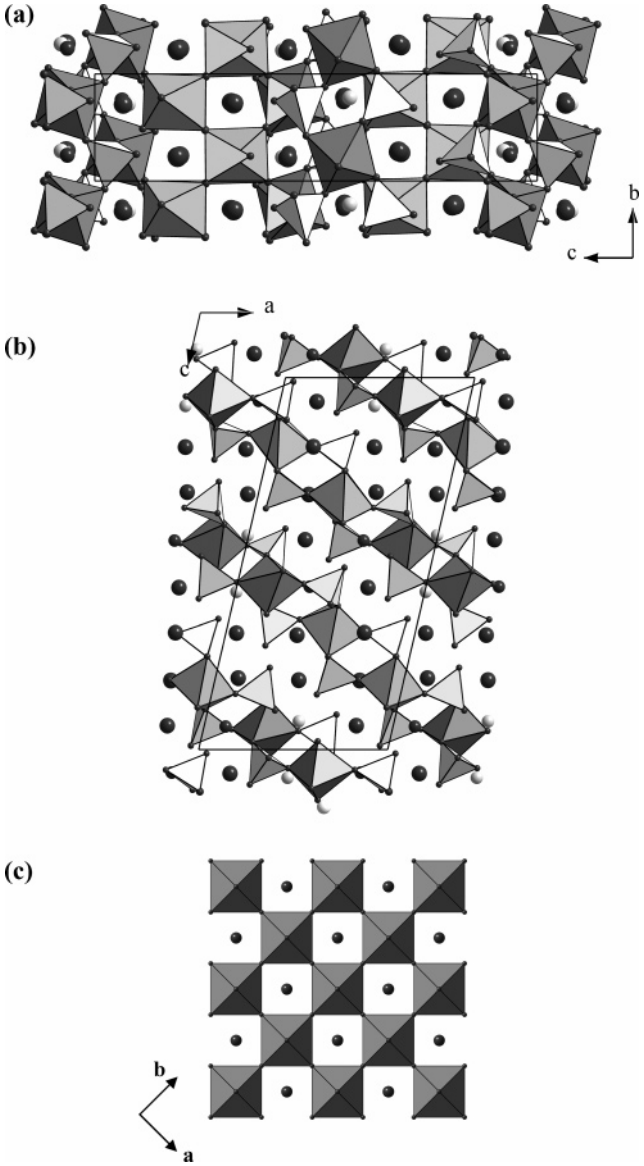

Figure 2. Projection views of (a) the structure of $KMnVO_4$ on the (100) plane, (b) the structure of $KMnVO_4$ on the (010) plane, and (c) the structure of the cubic perovskite ABO_3 on the (001) plane.

tunnels between the BO_6 octahedra. The structure of $KMnVO_4$ can be derived from the ideal cubic perovskite ABO_3 by occupying the A sites with potassium and manganese in a 2:1 ratio, and the B sites with manganese and vanadium in a 1:2 ratio, in an ordered fashion. In the A sites, the coordinate environments of potassium and manganese are drastically different from the ideal cuboctahedral O_{12} interstices. The potassium atoms are located in strongly distorted polyhedra with coordination numbers from 5 to 9 (with K−O distances shorter than 3.15 Å). The K−O distances range from 2.586(2) to 3.1030(15) Å. The short K3−O14 distance of 2.586(2) Å can be attributed to the fact that the O14 position is shared by the $V2O_4$ and $K3O_9$ polyhedra. Indeed, to accommodate a realistic V^{5+}−O14 distance, a short K3−O14 distance is induced. This steric strain is reflected in the relatively high value of ADP tensor parameters for the O14 position and explains the rather high value of the bond valence sum for K3 (Table 3). The manganese atoms occupy two different coordinate sites, that is, a tetrahedral site (Mn3) and a distorted octahedral site

Table 3. Main Interatomic Distances (Angstroms), Average Distances, Bond Valences (BV), and Bond Valence Sums (BVS) for $KMnVO_4$[n]

	distances	BV		distances	BV
Mn1−O6[b]	2.1414(13)	0.387	Mn4−O8	2.0675(15)	0.472
Mn1−O3	2.1526(14)	0.375	Mn4−O15	2.1464(15)	0.382
Mn1−O7	2.1851(13)	0.344	Mn4−O1	2.1259(11)	0.403
Mn1−O2[b]	2.2030(13)	0.328	Mn4−O2	2.2780(12)	0.267
Mn1−O4[c]	2.2326(12)	0.302	Mn4−O13[d]	2.2967(12)	0.254
Mn1−O1[a]	2.3496(13)	0.220	Mn4−O5	2.5488(11)	0.129
	⟨2.2106⟩	BVS = 1.956		⟨2.2438⟩	BVS = 1.907
Mn2−O12	2.1245(13)	0.405	K1−O5[b]	2.7474(14)	0.190
Mn2−O11	2.1535(13)	0.375	K1−O2	2.8430(15)	0.146
Mn2−O9[d]	2.1563(13)	0.372	K1−O11[b]	2.8540(15)	0.142
Mn2−O13[d]	2.2031(13)	0.327	K1−O13[i]	2.8942(14)	0.127
Mn2−O15	2.2046(12)	0.326	K1−O6	2.9081(14)	0.123
Mn2−O5	2.2240(13)	0.310	K1−O14[e]	2.9847(19)	0.100
	⟨2.1776⟩	BVS = 2.115	K1−O1	3.0705(15)	0.079
			K1−O8	3.0339(12)	0.087
V1−O10	1.6460(15)	1.529		⟨2.9168⟩	BVS = 1.012
V1−O3[e]	1.7130(12)	1.276			
V1−O15[b]	1.7392(13)	1.188	K2−O3[j]	2.6732(12)	0.232
V1−O7	1.7661(12)	1.105	K2−O10	2.7080(16)	0.211
	⟨1.7160⟩	BVS = 5.098	K2−O9[k]	2.7438(12)	0.191
			K2−O15[k]	2.7654(12)	0.181
V2−O14	1.645(2)	1.537	K2−O12[k]	2.7968(12)	0.166
V2−O4	1.7355(12)	1.200		⟨2.7374⟩	BVS = 0.981
V2−O1	1.7468(12)	1.164			
V2−O6	1.7660(12)	1.105	K3−O14	2.586(2)	0.293
	⟨1.7230⟩	BVS = 5.006	K3−O5[b]	2.7167(12)	0.206
			K3−O11[a]	2.7902(12)	0.169
V3−O16[g]	1.6981(15)	1.328	K3−O11[b]	2.8576(12)	0.141
V3−O12[b]	1.7115(12)	1.281	K3−O12[f]	2.8994(12)	0.126
V3−O11[f]	1.7169(12)	1.262	K3−O9[l]	2.9056(12)	0.124
V3−O9[b]	1.7192(12)	1.254	K3−O11[f]	2.9653(15)	0.105
	⟨1.7113⟩	BVS = 5.125	K3−O9	3.0504(15)	0.084
			K3−O12	3.1031(15)	0.072
V4−O8	1.6898(15)	1.358		⟨2.8748⟩	BVS = 1.320
V4−O5[b]	1.7093(12)	1.289			
V4−O13[b]	1.7267(12)	1.229	K4−O3	2.6412(15)	0.253
V4−O2[b]	1.7503(12)	1.153	K4−O9[k]	2.7886(15)	0.170
	⟨1.7189⟩	BVS = 5.029	K4−O12[m]	2.8003(15)	0.164
			K4−O7	2.8630(15)	0.139
Mn3−O16[c]	2.0471(15)	0.499	K4−O10	3.0251(15)	0.090
Mn3−O6[c]	2.0766(12)	0.461	K4−O10	3.0785(12)	0.077
Mn3−O4[h]	2.0804(12)	0.456	K4−O16	3.0949(16)	0.074
Mn3−O7	2.0981(12)	0.435		⟨2.8987⟩	BVS = 0.967
	⟨2.0755⟩	BVS = 1.851			

[a] $1-x, -y, 1-z$. [b] $1-x, 1-y, 1-z$. [c] $1-x, -y, -z$. [d] $-x, -1-y, -z$. [e] $-x, 1-y, -z$. [f] $-1/2+x, 1/2-y, -1/2+z$. [g] $1/2+x, -1/2-y, 1/2+z$. [h] $1-x, 1-y, -z$. [i] $1-x, 2-y, 1-z$. [j] $3/2+x, 1/2-y, 1/2+z$. [k] $1/2+x, 3/2-y, -1/2+z$. [l] $-1/2+x, 3/2-y, -1/2+z$. [m] $1/2+x, 1/2-y, -1/2+z$. [n] $BV = e^{(r_0-r)/b}$ with the following parameters:[29] $b = 0.37$ and r_0 (Mn^{II}−O) = 1.790, r_0 (V^{V}−O) = 1.803, and r_0 (K−O) = 2.132.

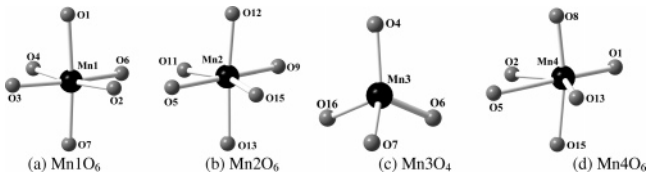

Figure 3. MnO_n ($n = 4-6$) polyhedra of $KMnVO_4$.

(Mn4) as shown in Figure 3. The average distance Mn3−O, equal to 2.076 Å, is close to the sum of the ionic radii (0.66 + 1.40 = 2.06 Å).[28] For Mn4, the coordinate polyhedron is a strongly distorted octahedra with one long Mn−O distance of 2.5487(11) and an average distance of 2.244 Å, close to the sum of the ionic radii (0.83 + 1.4 = 2.23 Å). This strong distortion can be attributed to a displacement of the Mn^{2+} cation away from the center of the octahedra to increase the distance between this cation and the neighboring V^{5+} cation in the V2 position. A short Mn−V distance is observed for both Mn3 and Mn4 positions with Mn3−V1 and Mn4−V4

(28) Shannon, R. D. *Acta Crystallogr.* **1976**, *A32*, 751.

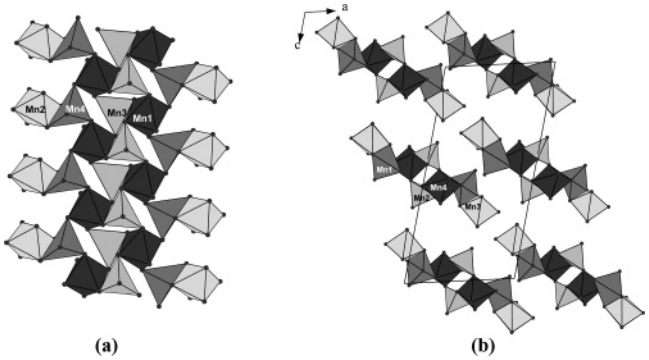

Figure 4. (a) Polyhedral representation of the connectivity between the MnO_n ($n = 4-6$) polyhedra in $KMnVO_4$, (b) Projection along the *b* axis of the unit cell filled only by the connected MnO_n polyhedra that form infinite chains that are running along the *b* axis.

distances of 2.957 and 2.941 Å, respectively. In the B sites, the manganese atoms occupy the octahedral sites, Mn1 and Mn2 (Figure 3), with average Mn−O distances of 2.218 and 2.178 Å, respectively, whereas the vanadium atoms occupy four different tetrahedral sites with average V−O distances of 1.716, 1.723, 1.711, and 1.719 Å for V1, V2, V3, and V4 sites, respectively. All of these polyhedra of the B sites are rather regular in shape.

Bond valence sum calculations for the manganese and vanadium atoms of $KMnVO_4$ confirm that they are present as Mn^{2+} and V^{5+} ions, respectively (Table 3).[29] The cation framework of $KMnVO_4$ is not very distorted compared to that of the ideal cubic perovskite ABO_3. This similarity is reflected in the simple relationships between the cell parameters of the monoclinic $KMnVO_4$ and those of the primitive cubic perovskite. Given the cell parameters of monoclinic $KMnVO_4$ as $\vec{a}_m$, $\vec{b}_m$, $\vec{c}_m$, and β, and those of the primitive cubic perovskite as $\vec{a}_p$, $\vec{b}_p$, and $\vec{c}_p$, it is found that $\vec{a}_m = 3\,\vec{c}_p$, $\vec{b}_m = -\vec{a}_p + \vec{b}_p$, $\vec{c}_m = 4\vec{a}_p + 4\vec{b}_p - \vec{c}_p$, and $\beta = 90° + \text{arctg}\ {}^{1}/_{(4\sqrt{2})} = 100.03°$. The cubic cell parameter is close to 4 Å, so that the corresponding monoclinic unit cell parameters are expected to be $a_m \approx 12$, $b_m \approx 5.7$, and $c_m \approx 23$ Å. The latter are comparable to those observed (Table 1). However, the oxygen framework of $KMnVO_4$ in part b of Figure 2 is strongly distorted from that of the ideal structure (next section) because the cations of different sizes present in the A sites (i.e., K^+ and Mn^{2+}) and the B sites (i.e., Mn^{2+} and V^{5+}) require different A−O and B−O bond lengths.

All of the MnO_n ($n = 4-6$) polyhedra share corners except for the $Mn2O_6$ and $Mn4O_6$ octahedra, which share one face (part a of Figure 4). These connected polyhedra form infinite chains that are running along the *b* axis (part b of Figure 4).

3.2. Structural Relationship with the Cubic Perovskite. To emphasize the relationship of the structure of $KMnVO_4$ to the cubic perovskite structure, the formula $KMnVO_4$ can be rewritten as $(K_2,Mn)[Mn,V_2]O_8\square_1$, which corresponds to the oxygen-deficient perovskite $A_3B_3O_8$ or $ABO_{3-\delta}$ with $\delta = {}^{1}/_{3}$. In the family of perovskite $A_nB_nO_{3n-1}$, the same composition exists for $n = 3$.[1] In this structure, there is a stacking of two octahedral layers and one tetrahedral layer. Among the most famous known oxygen-deficient perovskites, one can cite the brownmillerite,[2] $Ca_2Mn_2O_5$,[3] $La_2Ni_2O_5$,[4] and $LaNiO_2$.[17]

(29) Brese, N. E.; O' Keeffe, M. *Acta Crystallogr.* **1991**, *B47*, 192.

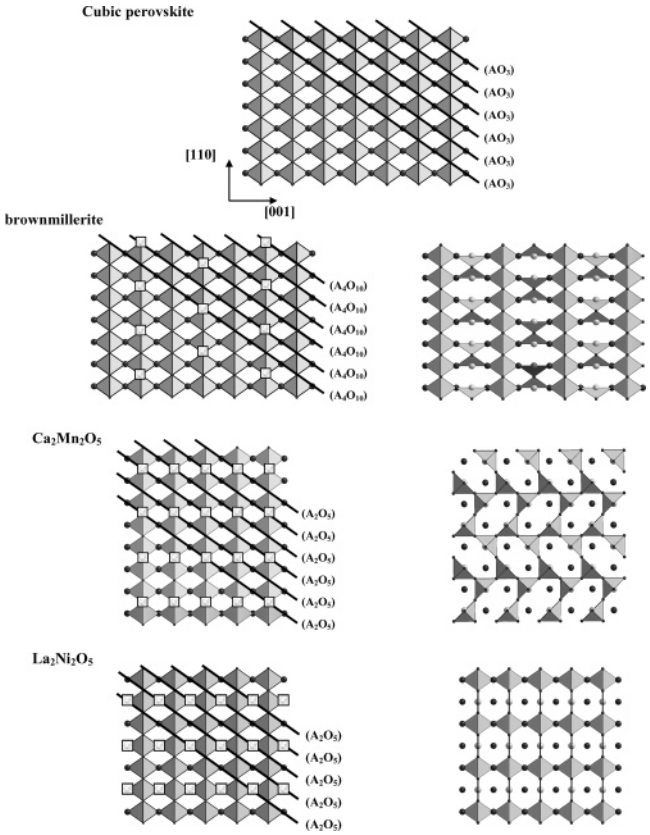

Figure 5. Projection views along the $[1\bar{1}0]$ direction of the cubic perovskite with oxygen vacancies, giving rise to the ideal brownmillerite, $Ca_2Mn_2O_5$, and $La_2Ni_2O_5$ structures. For $Ca_2Mn_2O_5$, the figure on the right part is a projection along the [001] direction.

A uniform description of the oxygen-deficient perovskites deriving from the cubic perovskite arrangement can be determined by considering that the ideal cubic perovskite ABO_3 is made of the stacking of close-packed AO_3 layers with a filling of the octahedral sites created between the layers with the B cations. This is shown in the projection view in Figure 5. In this view, the A cations and the apical oxygen atoms of the BO_6 octahedra are projected onto the same positions but with different heights along the $[\bar{1}10]$ direction. The ABO_3 layers are made of O_2 and AO rows running along the $[\bar{1}10]$ direction. In the case of the brownmillerite, in each AO_3 layer, one O_2 row in every four O_2 rows is removed (Figure 5). Then, the composition of the AO_3 layer becomes A_4O_{10}, with the general formula $A_4B_4O_{10}$ ($A_2B_2O_5$). When these rows of oxygen are removed, the octahedral site associated with this vacancy becomes a tetrahedral site, and a distortion of the oxygen framework is necessary to manage realistic angles. In the case of the $A_3B_3O_8$ compounds like $Ca_3Fe_2TiO_8$,[16] the same building principle is observed, in each AO_3 layer one O_2 row in every six O_2 rows is removed, given the general formula $A_6B_6O_{16} = A_3B_3O_8$. For these two structures, the octahedral site is transformed into a tetrahedral site by removing O_2 rows. In $Ca_2Mn_2O_5$, all of the manganese atoms are located in square pyramids of oxygen atoms. In the AO_3 layers, every two O_2 rows, half of the oxygen atoms are removed, and then all of the BO_6 octahedra become BO_5 square pyramids (Figure 5). To see the difference between an octahedral and a square pyramid site, a different projection has been chosen for this structure in Figure 5. For $La_2Ni_2O_5$, where nickel atoms are equally distributed over the square planar and the octahedral

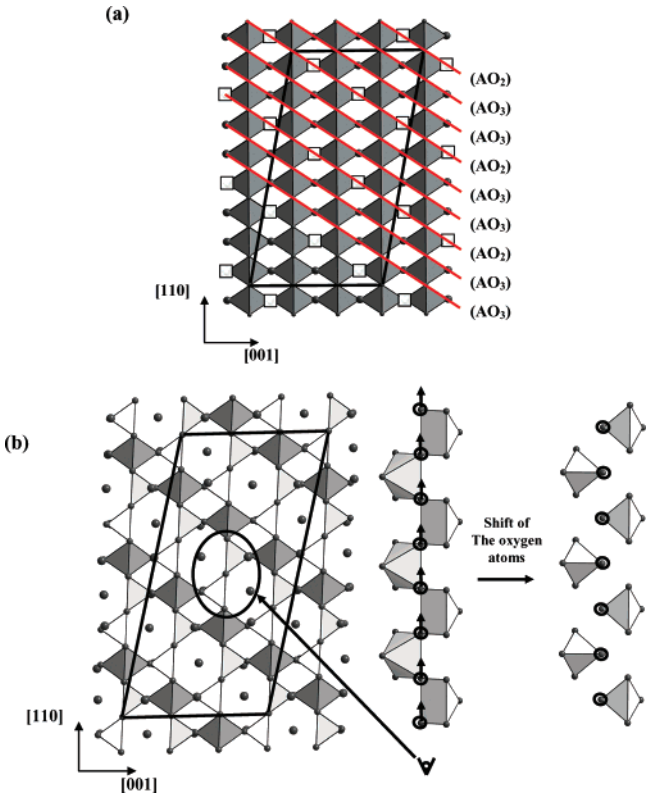

Figure 6. Projection views along the [1$\bar{1}$0] direction of (a) the cubic perovskite with oxygen vacancies, giving rise to the composition $A_3B_3O_8$ and (b) the ideal $KMnVO_4$ structure.

sites, in every two AO rows, oxygen atoms are removed, leading to a stacking of A_2O_5 layers (Figure 5). The reduction of this compound is achieved when all of the AO rows become A rows and all of the octahedral sites are transformed into square planar sites. For $KMnVO_4$, if every third row of oxygen atoms parallel to the [$\bar{1}$10] direction are removed as indicated in part a of Figure 6, there occurs a 3D network of corner-sharing BO_6 octahedra and BO_5 square pyramids. The resulting composition becomes $A_3B_3O_8$ (i.e., $ABO_{3-\delta}$ with $\delta = {}^1/_3$) with the stacking sequence $[(AO_3)(AO_3)(AO_2)]_\infty$. This type of oxygen-defect perovskite structure has not yet been reported. Finally, when the shared oxygen atoms of the corner-sharing BO_5 square pyramids are translated along the [$\bar{1}$10] direction by a $^1/_4$ period (the period along the [110] direction is about two times the O···O distance, i.e., ~5.6 Å), all of the BO_5 square pyramids become disconnected BO_4 tetrahedra, without changing the global composition (Figure 6b). To emphasize the existence of disconnected BO_4 tetrahedra, a different view is shown in part b of Figure 6. The projection view of the resulting structure is similar to that of the real structure of $KMnVO_4$ along the b direction in part b of Figure 2, without the strong distortion of the oxygen framework.

3.3. Magnetic Susceptibility and Specific Heat Measurements. The inverse molar magnetic susceptibility ($1/\chi_M$) of $KMnVO_4$ was plotted as a function of temperature T in Figure 7. Above 15 K, the $1/\chi_M$ versus T curve follows the Curie−Weiss law with $C = 4.28$ emu K/mol and $\theta = -75$ K. Below 15 K, the $1/\chi_M$ versus T curve can be fitted by the Curie−Weiss law with C ≈ 1 emu K/mol and a small θ value ($\theta = -6$ K). Specific heat measurements for $KMnVO_4$ exhibit a λ-type anomaly around 6 K in the C_p/T versus T plot (the upper inset of Figure 7). The $1/\chi_M$ versus T curve does not show any sign of a 3D antiferromagnetic ordering at $T = 6$ K. However, this temperature corresponds to the point at which the slope of the $\chi_M T$ versus T curve shows a significant change (the lower inset of Figure 7). The Curie constant observed in the $T > 15$ K region leads to an effective magnetic moment of 5.85 μ_B, which is in good agreement with the spin-only value of 5.92 μ_B expected for a high-spin Mn^{2+} (d^5) ion. The large negative Weiss temperature $\theta = -75$ K in the $T > 15$ K region corresponds to the occurrence of noticeable antiferromagnetic interactions between the Mn^{2+} ions. The slope of the $1/\chi_M$ versus T curve in the $T > 15$ K region ($C = 4.28$ emu K/mol) is reduced from that in the $T < 15$ K region by about 75% (C ≈ 1 emu K/mol). $KMnVO_4$ has four different types of Mn^{2+} ions in equal number, so that the change in the slopes of the $1/\chi_M$ versus T curve can be accounted for if substantial antiferromagnetic spin-exchange interactions in the $T > 15$ K region occur primarily among three of the four different types of Mn^{2+} ions. If the antiferromagnetic coupling between these ions is stronger than the available thermal energy in the $T < 15$ K region, then only one kind of Mn^{2+} ions will be left in $KMnVO_4$ to act paramagnetically in the $T < 15$ K region.

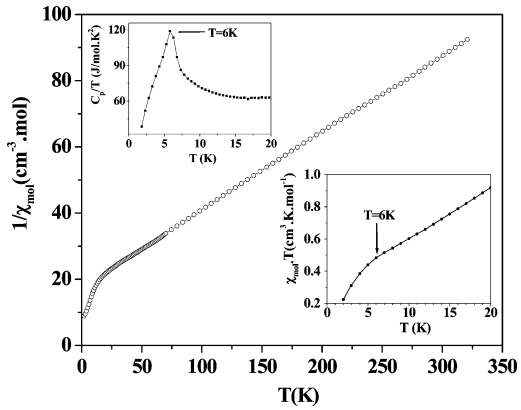

Figure 7. Inverse molar magnetic susceptibility $1/\chi_M$ of $KMnVO_4$ as a function of temperature T. The lower inset shows the corresponding $\chi_M T$ versus T plot, and the upper inset shows the C_p/T versus T plot, where C_p is the specific heat of $KMnVO_4$.

3.4. Spin Exchange Interaction. To verify the aforementioned implication, we estimate the relative strengths of the various Mn^{2+}···Mn^{2+} spin-exchange interactions in $KMnVO_4$ by performing a spin-dimer analysis based on extended Hückel tight-binding (EHTB) electronic structure calculations.[30] In this analysis, EHTB calculations are carried out for various spin dimers, that is, the structural units made up of two adjacent Mn^{2+} ions plus the oxygen atoms in their first coordinate spheres. The strength of a spin-exchange interaction between two spin sites is described by the spin-exchange parameter $J = J_F + J_{AF}$, where the ferromagnetic term J_F is positive and the antiferromagnetic term J_{AF} is negative. In general, J_F is a very small positive number so that the trends in the antiferromagnetic J values (i.e., $J < 0$) are well approximated by those in the corresponding J_{AF} values.[30] In the spin dimer analysis based on EHTB calculations, the trends in the J_{AF} values are estimated on the basis

(30) For recent reviews, see: (a) Whangbo, M.-H.; Koo, H.-J.; Dai, D. *J. Solid State Chem.* **2003**, *176*, 417. (b) Whangbo, M.-H.; Dai, D.; Koo, H.-J. *Solid State Sci.* **2005**, *7*, 827.

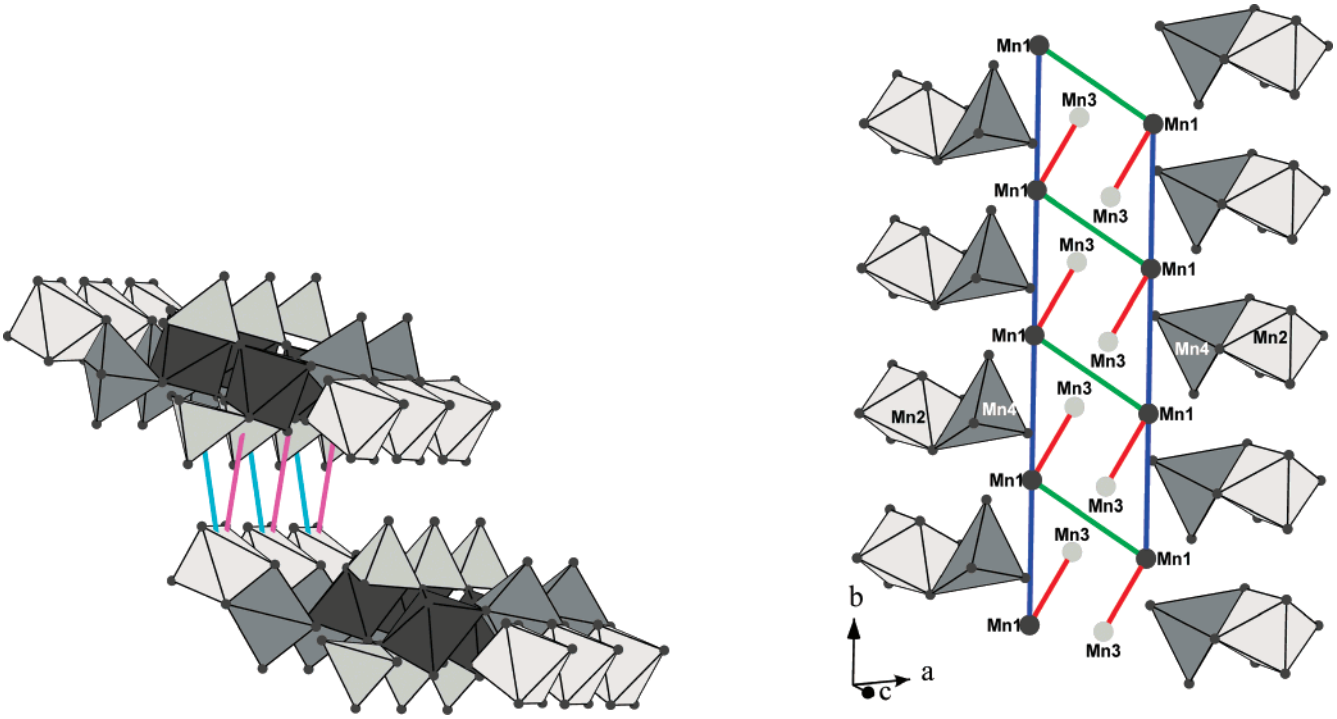

Figure 8. Simplified views of $Mn^{2+}\cdots Mn^{2+}$ spin-exchange paths in $KMnVO_4$. The $Mn^{2+}\cdots Mn^{2+}$ spin exchanges are represented by colored cylinders, which are defined in Table 4.

of the relationship, $J_{AF} \propto -\langle(\Delta\epsilon)^2\rangle$,[30] where the $\langle(\Delta\epsilon)^2\rangle$ term is calculated by performing EHTB calculations for a spin dimer. Each Mn^{2+} ion of $KMnVO_4$ has five singly occupied d-block levels ϕ_m ($\mu = 1-5$), that is, five magnetic orbitals. Thus, the $\langle(\Delta\epsilon)^2\rangle$ term is given by

$$\langle(\Delta\epsilon)^2\rangle \approx \frac{1}{5^2}\sum_{\mu=1}^{5}(\Delta\epsilon_\mu)^2$$

with $(\Delta\epsilon_\mu)^2 = (\Delta e_\mu)^2 - (\Delta e_\mu^0)^2$,[30] where Δe_μ^0 is the energy difference between the magnetic orbitals ϕ_m representing each spin site of the spin dimer ($\Delta e_\mu^0 = 0$ if the two spin sites are equivalent), and Δe_μ is the energy split that results when two magnetic orbitals ϕ_m ($\mu = 1 - 5$) on adjacent spin sites interact.

In magnetic oxides of transition metal ions M, the spin-exchange interactions between adjacent metal ions may take place through M−O−M superexchange (SE) paths and/or M−O···O−M super-superexchange (SSE) paths.[30] When the O···O contact of an SSE path M−O···O−M forms an edge of an $M'O_4$ tetrahedron containing a d^0 ion (i.e., $M' = V^{5+}$, Mo^{6+}), it is crucial to include the $M'O_4$ tetrahedron in the structural unit representing the spin dimer because such M−O···O−M spin-exchange interactions are strongly affected by the O−M′-O bridge.[31−34] Therefore, in our EHTB calculations[35] for the $\langle(\Delta\epsilon)^2\rangle$ values of various spin dimers in $KMnVO_4$, all of the VO_4 tetrahedra associated with the Mn−O···O−Mn spin-exchange paths were included in the structural units representing the spin dimers. Results of our calculations for all of the nearest-neighbor spin-exchange interactions between four different manganese atoms are summarized in Table 4.

Table 4 reveals that the spin-exchange interactions associated with the Mn4 sites are negligible compared with those not involving the Mn4 sites. The Mn4 sites lead to very weak spin-exchange interactions with the neighboring manganese sites (i.e., Mn1, Mn2, Mn3, or Mn4 sites) because the $Mn4O_6$ square pyramids are strongly distorted so that the magnetic orbitals of a given Mn4 site have poor overlap with those of its neighboring manganese site. The strong antiferromagnetic spin-exchange interactions between the

Table 4. Mn···Mn Distances and $\langle(\Delta\epsilon)^2\rangle$ Values of Various $Mn^{2+}\cdots Mn^{2+}$ Spin Exchange Paths in $KMnVO_4$[a]

spin exchange path	Mn···Mn[b]	$\langle(\Delta\epsilon)^2\rangle$
Mn1···Mn1	5.272	210 (0.07)
Mn1···Mn1	5.378 (J_5, white)	990 (0.33)
Mn1···Mn1	5.645 (J_2, blue)	2600 (0.87)
Mn1···Mn2	5.572	640 (0.21)
Mn1···Mn2	5.707	230 (0.08)
Mn1···Mn3	3.415 (J_1, red)	3000 (1.00)
Mn1···Mn3	3.431	300 (0.10)
Mn1···Mn3	3.758	760 (0.25)
Mn1···Mn4	3.777	24 (0.01)
Mn1···Mn4	3.780	72 (0.02)
Mn2···Mn2	5.645	50 (0.02)
Mn2···Mn2	5.702	40 (0.01)
Mn2···Mn3	6.577 (J_1, pink)	1200 (0.40)
Mn2···Mn3	6.648 (J_3, cyan)	1600 (0.53)
Mn2···Mn4	3.142	320 (0.11)
Mn3···Mn3	5.645	420 (0.14)
Mn3···Mn4	4.697	580 (0.19)
Mn4···Mn4	5.241	50 (0.02)
Mn4···Mn4	5.351	80 (0.03)
Mn4···Mn4	5.645	420 (0.14)

[a] Mn···Mn distances and $\langle(\Delta\epsilon)^2\rangle$ values are in units of Å and (meV),[2] respectively. The relative values of $\langle(\Delta\epsilon)^2\rangle$ with respect to the largest one are given in parentheses. [b] The spin-exchange parameters J_1-J_5 are used in Figure 7 to indicate the spin-exchange paths involved, and the colors in parentheses refer to those of the Mn···Mn cylinders in Figure 8.

(31) Dai, D.; Koo, H.-J.; Whangbo, M.-H. *Inorg. Chem.* **2004**, *43*, 4026.
(32) Koo, H.-J.; Whangbo, M.-H. *Inorg. Chem.* **2006**, *45*, 4440.
(33) Kaul, E. E.; Rosner, H.; Yushankhai, V.; Sichelschmidt, J.; Shpanchenko, R. V.; Geibel, C. *Phys. Rev. B* **2003**, *67*, 174417.
(34) Duc, F.; Millet, P.; Ravy, S.; Thiollet, A.; Chabre, F.; Ghorayeb, A. M.; Mila, F.; Stepanov, A. *Phys. Rev. B* **2004**, *69*, 094102.
(35) Our calculations were carried out by employing the *SAMOA* (Structure and Molecular Orbital Analyzer) program package (Dai, D., Ren, J., Liang, W., Whangbo, M.-H http://chvamw.chem.ncsu.edu/, 2002).

Mn1, Mn2, and Mn3 sites give rise to the spin lattice depicted in Figure 8, in which all of the adjacent Mn^{2+} ions are antiferromagnetically coupled. Therefore, the substantial antiferromagnetic spin-exchange interactions of $KMnVO_4$ observed in the $T > 15$ K region originate primarily from the $Mn^{2+}\cdots Mn^{2+}$ spin-exchange interactions involving only the Mn1, Mn2, and Mn3 sites and the paramagnetic behavior of $KMnVO_4$ observed in the $T < 15$ K region from the isolated Mn^{2+} ions of the Mn4 sites. This finding is consistent with the magnetic susceptibility and specific heat data of $KMnVO_4$.

4. Conclusions

In summary, $KMnVO_4$ is a magnetic oxide that represents a new type of ordered oxygen-deficient cubic perovskite $ABO_{3-\delta}$ with $\delta = {}^1/_3$, in which high-spin Mn^{2+} ions occupy four different crystallographic sites among the A and B sites. Substantial antiferromagnetic spin-exchange interactions occur only among three of the four different types of Mn^{2+} ions. The antiferromagnetic ordering among these three types of Mn^{2+} ions is responsible for the specific heat anomaly found in the C_p/T versus T plot at $T = 6$ K, and the remaining Mn^{2+} ions not involved in antiferromagnetic coupling are responsible for the paramagnetic behavior of $KMnVO_4$ below 15 K. This paramagnetic contribution dominates at low temperatures, which explains why the susceptibility shows no maximum at $T = 6$ K.

Acknowledgment. The work at NCSU was supported by the Office of Basic Energy Sciences, Division of Materials Sciences, U.S. Department of Energy, under Grant DE-FG02-86ER45259.

Supporting Information Available: Table of the anisotropic displacement factors for $KMnVO_4$. This material is available free of charge via the Internet at http://pubs.acs.org.

CM070452B